


Nanometer-scale chip formation and surface integrity of pure titanium in diamond turning

Mehdi Heidari¹ · Jiwang Yan¹ 

Received: 2 August 2017 / Accepted: 27 September 2017 / Published online: 25 October 2017
© Springer-Verlag London Ltd. 2017

Abstract Titanium is attracting great attentions in aerospace and medical applications where high surface quality plays an important role in improving the product performance. For developing nano-precision machining technology for titanium, clarification of the nanometer-scale chip formation mechanism is essential. In this study, the surface formation mechanism of pure titanium in ultraprecision cutting tests using single-crystal diamond tools was investigated. The results demonstrated that decreasing undeformed chip thickness from the micrometer scale down to the nanometer scale had profound impacts on the shear angle, specific cutting force, and chip morphology. Chip tearing phenomenon occurred when undeformed chip thickness is smaller than a critical value (~ 100 nm), which significantly affected the chip morphology and machined surface integrity. In nanometer-scale cutting, tool feed mark is no longer a major reason of surface roughness; instead, material plucking, debris, scratches, and chip adhesion influenced the surface integrity. The high pressure generated in the nanometer-scale cutting caused a hardness increase in workpiece material and promoted workpiece material adhesion to the tool surface, as well as tool wear.

Keywords Pure titanium · Ultraprecision cutting · Diamond turning · Chip formation · Surface roughness · Tool wear

✉ Jiwang Yan
yan@mech.keio.ac.jp

¹ Department of Mechanical Engineering, Keio University, Hiyoshi 3-14-1, Kohoku-ku, Yokohama 223-8522, Japan

1 Introduction

Titanium is attracting more and more attentions in various areas such as aerospace and medical applications [1, 2]. However, titanium is very difficult to machine owing to its low thermal conductivity, high strength, and low modulus of elasticity [3–5]. To overcome the difficulties in machining titanium and its alloys, extensive studies have been done in the past decades on their cutting mechanism. These researches can be roughly classified into three main categories: first, studies on fundamental cutting mechanism and chip formation and their relationship to mechanical properties of titanium [6–12]; second, researches on the optimization of machining conditions to enhance the machinability of titanium [13–16]; and third, researches on tool wear mechanism and surface integrity in titanium machining [17–20]. However, most of the previous cutting experiments were conducted in the micrometer scale or larger. The research work on the nanometer-scale ultraprecision cutting of titanium is very limited.

Ultraprecision cutting, which is often referred to as single-point diamond turning (SPDT), is an established technology for manufacturing micro-structured surfaces with nanometer-level form accuracy, high surface quality, and complex shapes. Zareena and Veldhuis [21] investigated the tool wear mechanism in ultraprecision cutting of titanium and Ti-6Al-4V using single-crystal diamond tools. They found that high temperature and high pressure at the tool-chip interface initiated the chemical interaction between titanium and diamond. Schneider et al. [22, 23] analyzed the surface integrity in titanium cutting using quick-stop orthogonal cutting tests and considered the effect of undeformed chip thickness (ranging from 0.1 to 10 μm) on cutting forces. Ruibin and Wu [24] investigated the influence of machining parameters on surface roughness and cutting forces. Colafemina et al. [25] studied surface damage in machining of titanium and found the

Table 1 Mechanical properties of titanium workpiece

Ultimate tensile strength (MPa)	370
Yield strength (MPa)	300
Vickers hardness (HV)	145

surface damage was due to the material delamination phenomenon.

However, to date, there is no available literature on chip formation mechanism in diamond turning of pure titanium down to the nanometer scale. Regarding demands for nano-precision surfaces that have rapidly increased in advanced engineering fields, it is necessary to understand the cutting mechanism in the nanometer scale. The aim of the present research is to study the fundamental characteristics of cutting mechanism and chip formation behavior in diamond turning of titanium down to the nanometer-scale undeformed chip thickness. For this purpose, the changes in shear angle, specific cutting forces, and chip morphology as undeformed chip thickness decreases have been investigated. The key factors affecting the chip integrity, surface quality, and tool wear have been clarified.

2 Material and methods

2.1 Material

The workpiece material used in the experiments was an alpha-type commercial pure titanium (sample size

20.0 mm × 15.0 mm × 10.0 mm) with purity of 99.8% and nominal max composition (wt%) given as Fe, 0.25; O, 0.2; C, 0.08; N, 0.03; and H, 0.13. Table 1 shows the mechanical properties of the titanium samples.

2.2 Experimental setup and conditions

The machining experiments were carried out on a three-axis control ultraprecision machine, NACHI ASP-15 (NACHI-FUJIKOSHI CORP). Figure 1 shows a schematic diagram of the diamond turning setup. The machine has two perpendicular linear tables supported by high-stiffness hydrostatic bearings driven by servomotors. To prevent from backlash movements in the machine rotary table, the table is supported by hydrostatic bearings and driven by a friction drive. The machine is equipped with laser hologram scales to accurately position all of these tables. The linear tables can be moved at 1 nm per step and the rotary table is able to rotate with an angular resolution of 0.00001°.

A workpiece holder was designed and fabricated to fix the workpiece to the spindle. This holder uses a sliding mechanism to adjusting the distance between the workpiece and the center of spindle. The workpiece was fixed using three screws to the holder which is then vacuum chucked to the machine spindle, as shown in Fig. 1. In addition, to keep dynamic balance during spindle rotation, a metal piece was fixed on the opposite side of the workpiece. A piezoelectric dynamometer (Kistler 9256C2) was mounted below the tool to

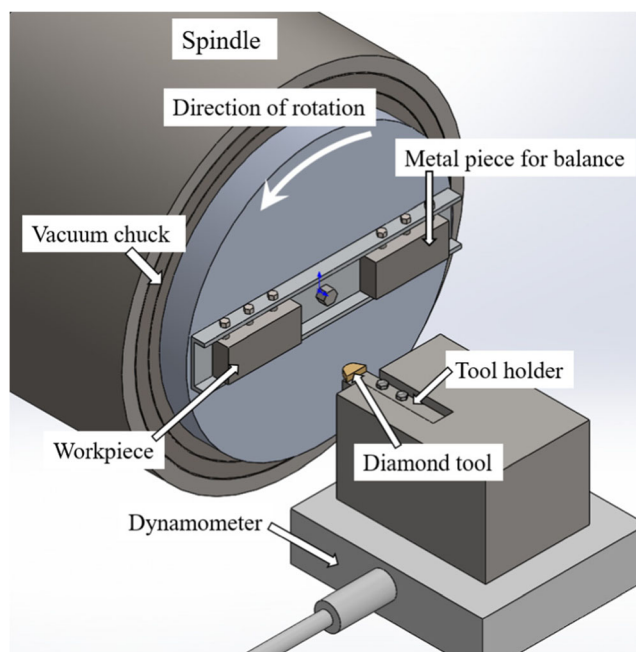


Fig. 1 Schematic diagram of experimental setup

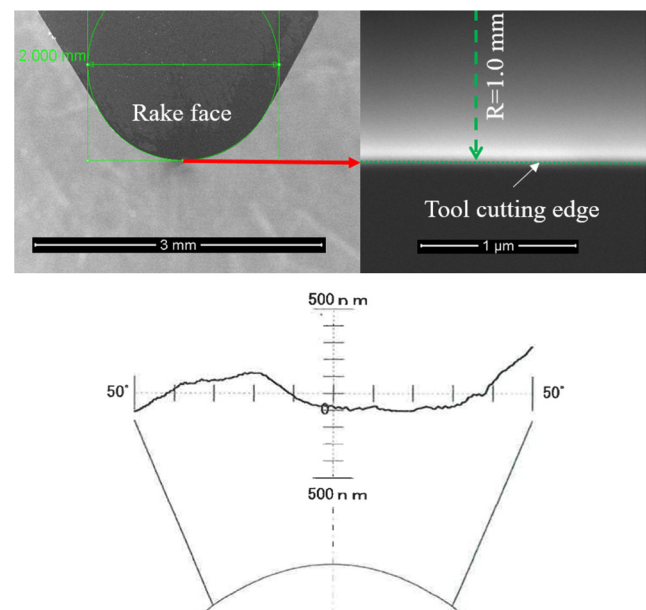


Fig. 2 SEM micrograph and contour profile of a diamond tool edge

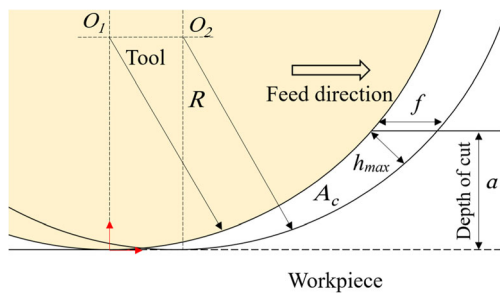


Fig. 3 Cutting model of a round-nosed tool

measure cutting forces during the cutting tests. To guarantee the accuracy of the experimental results, all cutting tests were repeated twice at the same conditions. Commercially available single-crystal diamond tools with a nose radius of 1.0 mm, tool edge radius of ~ 100 nm, and rake and clearance angles of 0° and 8°, respectively, were used in these experiments. Figure 2 shows SEM images and contour profiling error of a single-crystal diamond tool. The tool faces and the edge are extremely smooth. The geometrical error over a window angle of 100° is ~ 380 nm; thus, in the actually used range of tool edge, the profile accuracy of the tool is in the nanometric scale.

Four different feed rates, 1, 10, 50, and 100 μm/rev, and two different depths of cut, 5 and 15 μm, were used to cut eight concentric areas on each sample. Since the distance of each area from spindle center is different, spindle rotation rate was adjusted for each area to get the same cutting speed (50 m/min) in all tests.

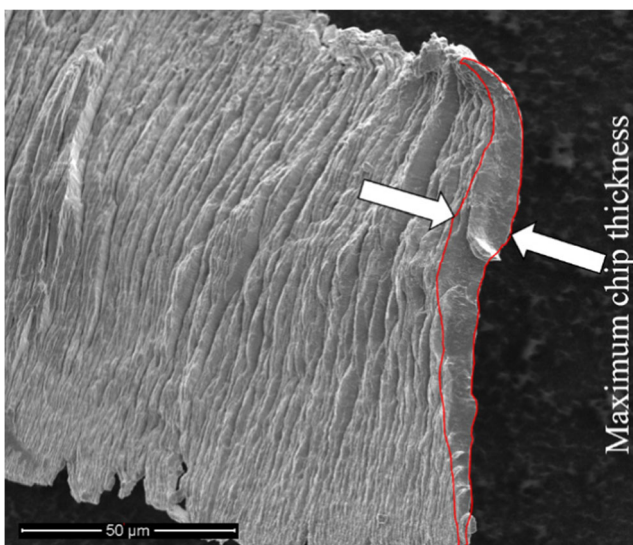


Fig. 4 SEM micrograph of chip ($f = 100 \mu\text{m}/\text{rev}$, $a = 5 \mu\text{m}$) used for measuring chip thickness

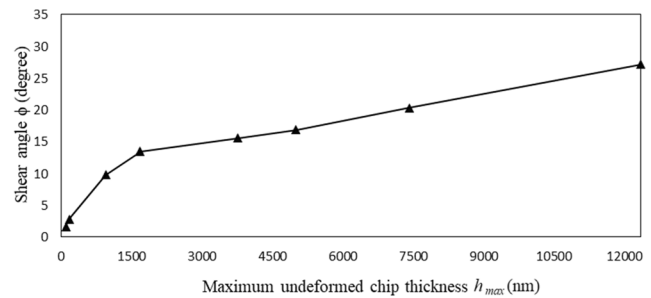


Fig. 5 The variations in shear angle as h_{max} decreases

In order to evaluate the machined surface texture, a white light interferometer was used and the surface profile was analyzed by the Talysmap software (Taylor Hobson Ltd.). A scanning electron microscope (SEM, Model Inspect S50) was used to observe the chips, the machined surfaces, and tool wear. Some of the SEM images were then analyzed by the ImageJ software. To evaluate micro-hardness variations, hardness measurements were performed using a micro Vickers hardness tester (Shimadzu HMV-G21S) by applying a load of 1 N for 10 s on selected specimens.

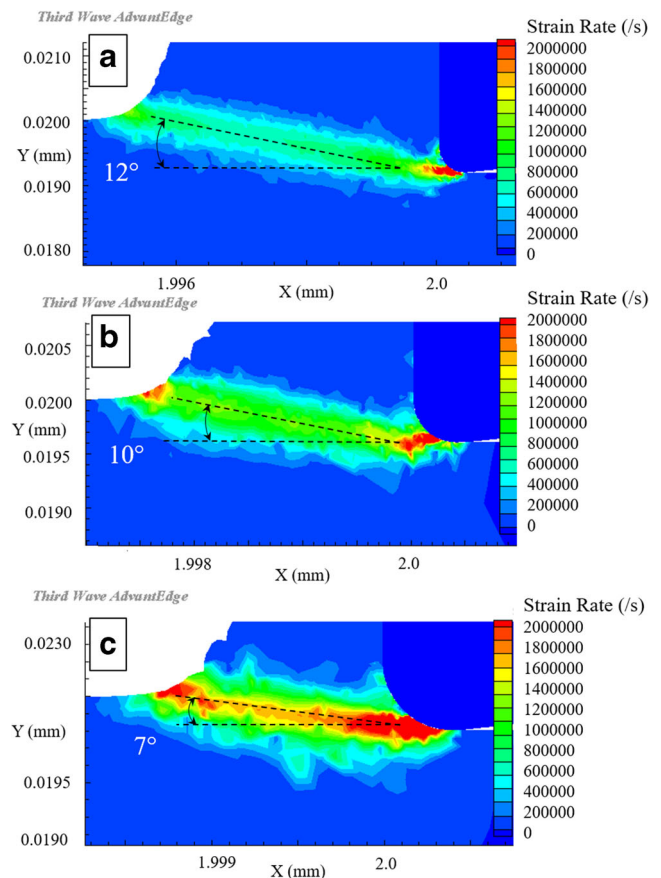


Fig. 6 FE simulations of strain rate distribution at three different depths of cut: $a = 2.0 \times r$ (a), $a = 1.0 \times r$ (b), and $a = 0.5 \times r$ (c)

2.3 Cutting models

Figure 3 shows a schematic model for diamond turning with a round-nosed tool, where the maximum undeformed chip thickness (h_{\max}) is an important parameter to evaluate the cutting performance. h_{\max} can be calculated from the tool nose radius R , depth of cut a , and tool feed rate f , using the following equation when $f < \sqrt{2Ra - a^2}$ [26, 27].

$$h_{\max} = R - \sqrt{R^2 + f^2 - 2f\sqrt{2Ra - a^2}} \quad (1)$$

When $f \geq \sqrt{2Ra - a^2}$, however, h_{\max} is equal to the depth of cut (a).

For instance, at $f = 1 \mu\text{m}/\text{rev}$ and $a = 5 \mu\text{m}$, the undeformed chip thickness over the entire cutting region changes from 0 to 99 nm. Regarding machining conditions used in this study, the maximum undeformed chip thickness ranged from 99 to 12,331 nm.

2.4 Finite element simulation

To assist understanding the material removal mechanism of titanium, the cutting-induced pressure and strain rate distributions in the cutting area were investigated by using AdvantEdge, a finite element (FE) machining simulation program produced by Third Wave Systems, USA. Two-dimensional simulations of orthogonal cutting were

performed; thus, the undeformed chip thickness was the same as the depth of cut. The tool rake angle, relief angle, and cutting speed used in the simulations were the same as those used in the experiments. Using a tool edge radius smaller than 100 nm, as used in the experiment, was extremely time-consuming in simulations, so an edge radius (r) of 400 nm was used. Accordingly, larger depth of cuts (a) was used in the simulation to keep the same ratio of depth of cut to edge radius as that in the experiments. The modified power law constitutive model was used to establish the material property model for titanium.

3 Results and discussion

3.1 Shear angle

Shear angle can be found utilizing the measured chip ratios using Eq. (2), which is derived from the ratio (r_c) of undeformed chip thickness (h) to the chip thickness (l). Concerning the shear angle changes along the round edge of the tool, in this study, shear angle was calculated based on maximum chip thickness measured using ImageJ software by analyzing the SEM images of chips, as shown in Fig. 4.

$$\varphi = \text{atan}(r_c) \quad (2)$$

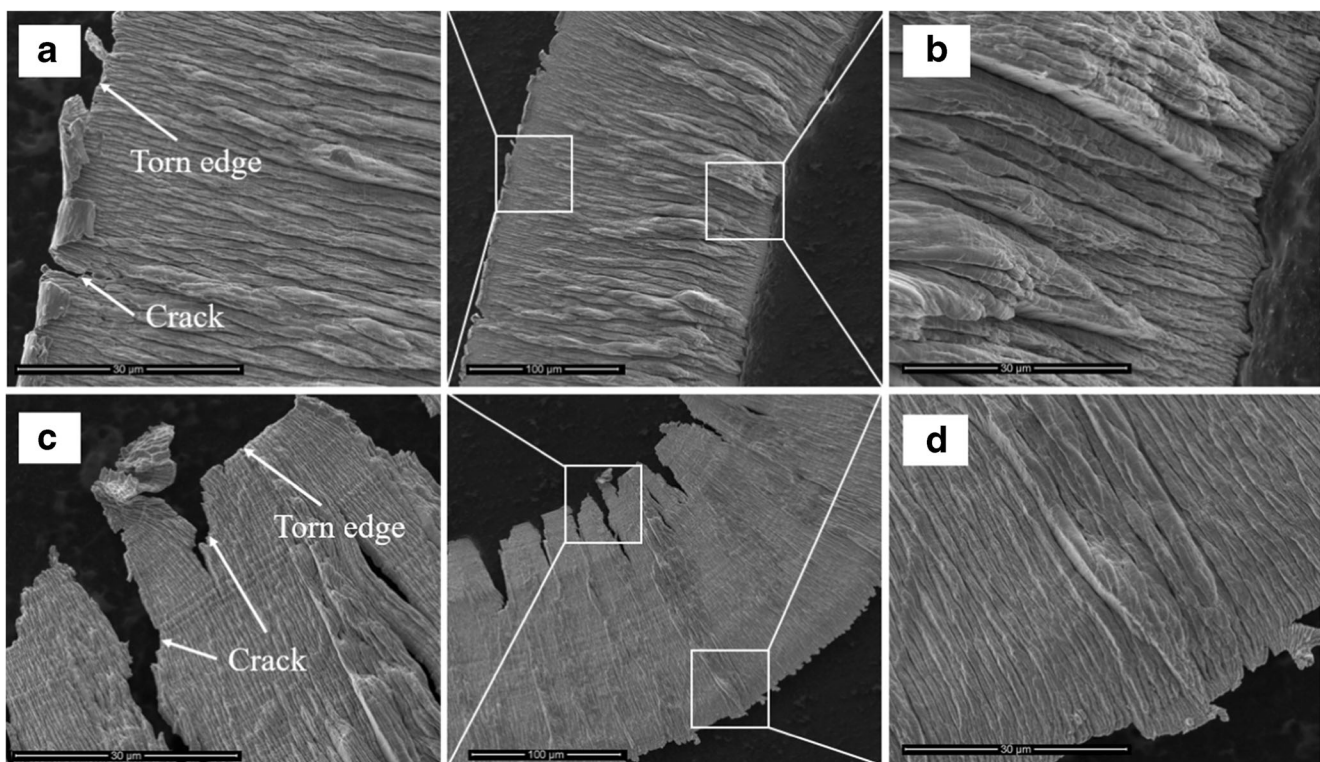


Fig. 7 SEM micrographs of chip obtained at $h_{\max} = 7405 \text{ nm}$ ((a), (b)) and $h_{\max} = 1679 \text{ nm}$ ((c), (d))

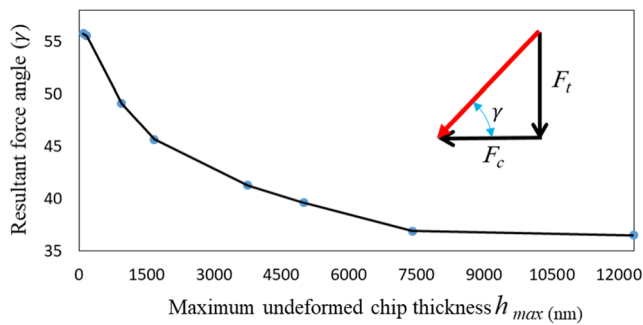


Fig. 8 Change of resultant force angle with h_{max}

As shown in Fig. 5, the shear angle decreases as h_{max} decreases; especially when $h_{max} < 1676$ nm, the shear angle decreases sharply.

FE modeling of cutting at different undeformed chip thicknesses also confirms that shear angle decreases as h_{max} decreases, as presented in Fig. 6. The simulation results also proved that as undeformed chip thickness decreased, the narrow shear plane gradually converted to a broad shear zone.

3.2 Chip morphology

Figure 7((a)–(d)) shows the chips obtained at $h_{max} = 7405$ nm and $h_{max} = 1679$ nm, respectively. In the figure, chip edge tearing phenomenon is observed. The chip tearing is more significant in Fig. 7((a), (c)) (left side of chip) compared to Fig. 7((b), (d)) (right side of chip). This result demonstrated that a larger cutting width with smaller undeformed chip

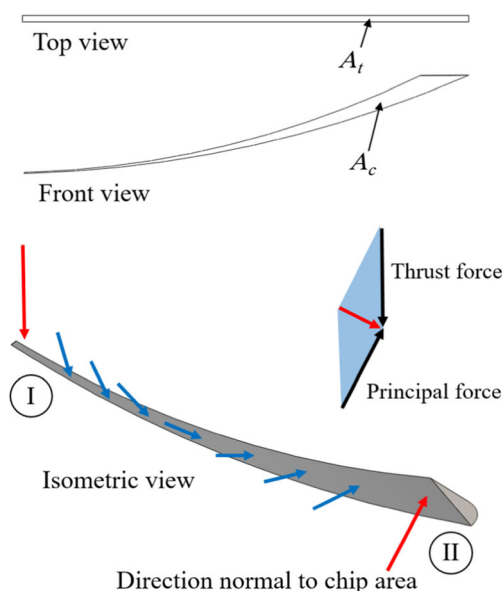


Fig. 9 Schematic model for tool-workpiece contact area

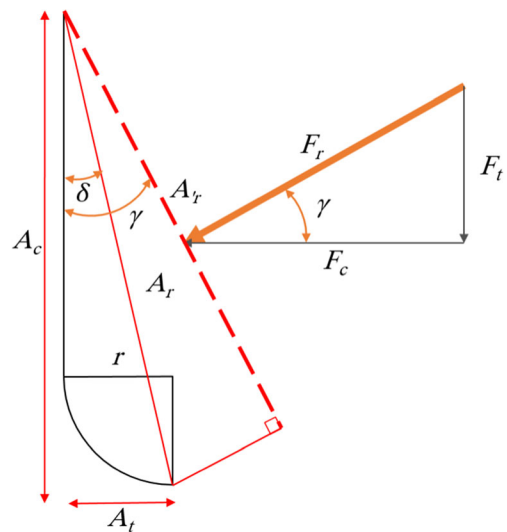


Fig. 10 Model for calculating specific cutting force

thickness caused more severe chip tearing. Apart from chip tearing, cracks were generated on the left side chip edge in Fig. 7((a), (c)).

In order to understand the chip tearing phenomenon, the change in cutting force direction with undeformed chip thickness was calculated. Figure 8 shows the change of resultant force angle with h_{max} . As undeformed chip thickness decreases, resultant force angle (γ) increases from 36° at $h_{max} = 12,331$ nm to 57° at $h_{max} = 99$ nm. Similarly, as undeformed chip thickness decreases from the uncut surface to the cut surface in Fig. 3, the resultant force direction will change significantly.

Figure 9 shows a schematic three-dimensional model for tool-workpiece contact area. While the area of the plane normal to principal force decreases from right side “II” to left side “I,” the area of the plane normal to thrust force, which is determined by tool edge radius, remains constant along the tool edge. Thus, the resultant force in the region close to “II” is mostly parallel to cutting direction, while that around “I” is directed toward the workpiece surface.

The change of resultant force direction along the tool edge as shown in Fig. 9 leads to different chip formation behaviors.

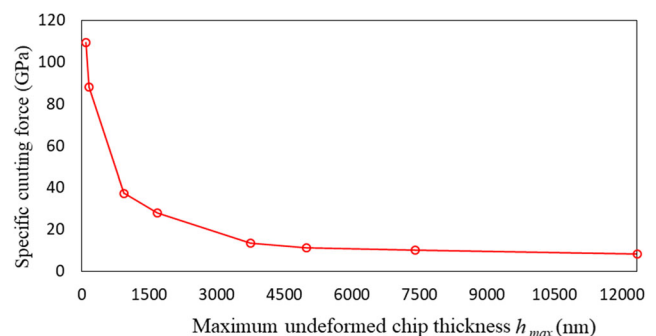


Fig. 11 Change of specific cutting force with h_{max}

The force component vertical to the workpiece surface near region “I” causes chip tearing (Fig. 7((a), (c))). However, the force component parallel to cutting direction near region “II” causes continuous chip flow (Fig. 7((b), (d))).

Next, the specific cutting force [28–30], i.e., the ratio of the resultant force to the tool-workpiece contact area projected on the plane normal to the resultant force (Fig. 10), was calculated using following equations.

$$F_{sp} = \frac{F_r}{A'_r} \tag{3}$$

$$F_r^2 = F_c^2 + F_t^2 \tag{4}$$

$$\tan\gamma = \frac{F_t}{F_c}, \quad \tan\alpha = \frac{A_t}{A_c}, \quad A'_r = A_r \cos(\gamma - \delta) \tag{5}$$

$$A_t = r \times \left[2\pi R \left(\frac{\alpha + \beta}{360} \right) \right] \text{ (see Fig.23(a))} \tag{6}$$

$$A_c = \left(\int_{\frac{x}{R}}^{\sqrt{\frac{2Ra-a}{R}}} R - \sqrt{R^2 - x^2} dx \right) + (f \times a) - \left(\int_{\frac{x-f}{R}}^{\sqrt{\frac{2Ra-a+f}{R}}} R - \sqrt{R^2 - (x-f)^2} dx \right) \tag{7}$$

$$= \left[-\frac{1}{2}R^2 \left(\arcsin\left(\frac{x}{R}\right) + \frac{1}{2} \sin\left(2\arcsin\left(\frac{x}{R}\right)\right) \right) + Rx + C_1 \right]$$

$$+ [f \times a] - \left[-\frac{1}{2}R^2 \left(\arcsin\left(\frac{x-f}{R}\right) + \frac{1}{2} \sin\left(2\arcsin\left(\frac{x-f}{R}\right)\right) \right) + R(x-f) + C_2 \right]$$

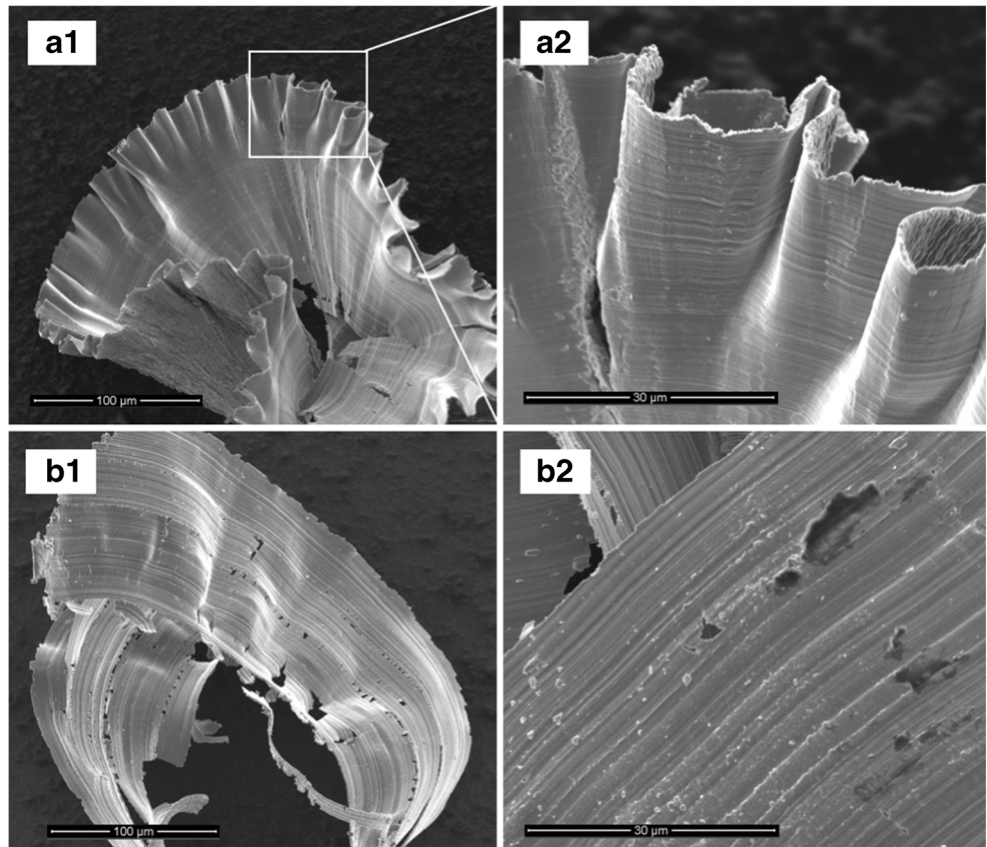
[27]

where F_{sp} is specific cutting force, F_r is resultant force, F_c is principal force, F_t is thrust force, A_c is area normal to principal force, A_t is area normal to thrust force and derived from multiplication of tool edge radius (r) in the width of chip, A_r is the resultant area of A_c and A_t , A'_r is area of A_r normal to resultant force, and γ and α are angles between A'_r and A_r and the vertical direction. It should be pointed out that as tool wears out, the tool edge radius increases, and consequently, cutting force increases. To reduce the effects of tool wear on specific cutting force results, a new tool was used for a very short cutting distance (~ 75 m) for force measurement.

Figure 11 shows the results of specific cutting force with respect to h_{max} . As h_{max} decreases, the specific cutting force increases slightly, and then sharply increases, especially when h_{max} approaches the sub-micrometer level. This sharp rise in specific cutting force at very small undeformed chip thickness contributes to the chip tearing phenomenon.

For the “II” side of the chip, instead of chip tearing, chip edge wrinkle was observed at a small h_{max} , when a worn tool was used. As shown in Fig. 12((a1), (a2)), chip wrinkle is found at the upper side edge of chips formed at $h_{max} = 172$ nm by a tool after a cutting distance of 250 m. In contrast, the chip generated by a tool after

Fig. 12 SEM micrographs of chips formed by a tool after a cutting distance of 250 m ((a1), (a2)) and 75 m ((b1), (b2)) at $h_{max} = 172$ nm



a cutting distance of 75 m has no edge wrinkles, as shown in Fig. 12((b1), (b2)). Chip wrinkling is a result of local elongation of a chip due to high strain squeezing, which is accelerated as the tool wears out. However, the high-strain band is very narrow compared with the “I” side, which is insufficient to cause chip tearing.

After repetitive experiments and measurement of lengths of torn edge and chip widths as shown in Fig. 13, it was found that chip tearing occurred only when the undeformed chip thickness is smaller than a critical value ~ 100 nm, which is approximately equal to the tool edge radius of a commercially available diamond tool.

Under a feed rate of $1 \mu\text{m}/\text{rev}$ and a depth of cut of $5 \mu\text{m}$, the maximum undeformed chip thickness was 99 nm; thus, chip tearing occurred all over the tool edge, as shown in Fig. 14.

As undeformed chip thickness is further decreased below a minimum chip thickness (t_{\min}), a kind of transition to plowing occurs and no chip formation takes place. To determine the minimum uncut chip thickness experimentally, a set of experimental tests were carried out at a feed rate of $0.2 \mu\text{m}/\text{rev}$ and different depths of cut ranging from 0.5 to $50 \mu\text{m}$ to produce a maximum undeformed chip thickness from 5 to 50 nm.

At a maximum undeformed chip thickness $h_{\max} = 10$ nm, small particles were generated, as shown in Fig. 15((a1), (a2)), while no continuous chips were found. As h_{\max} increased to 30 nm, short continuous chips were generated lamella structure (Fig. 15((b1), (b2))). This result indicates that the minimum chip thickness (t_{\min}) is between 10 and 30 nm. Longer continuous chips with regular lamella structures were observed at $h_{\max} = 50$ nm (Fig. 15((c1), (c2))). This indicates that when undeformed chip thickness is less than 50 nm, the workpiece

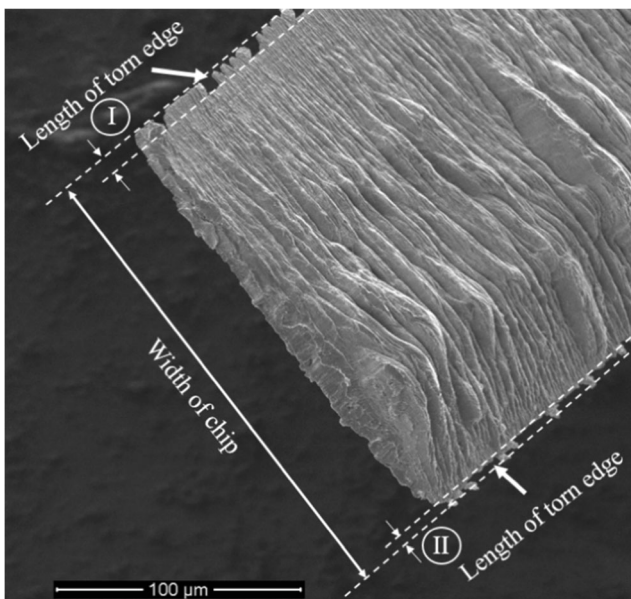


Fig. 13 SEM micrograph of deformed chip profile ($h_{\max} = 7405$ nm)

material deformation is mainly plowing, where plastic deformation occurs in a broad zone rather than a shear plane. Thus, the stable formation of long and continuous chips becomes difficult, causing the aforementioned chip tearing phenomenon.

Many researchers have proposed theoretical models to determine the minimum uncut chip thickness [31–39]. Most of these models are derived on the basis of friction coefficient and tool edge radius. One of the widely used models, proposed by Son et al. [40], is shown in Eq. (8).

$$t_{\min} = r \times \left(1 - \cos\left(\frac{\pi}{4} - \frac{\rho}{2}\right) \right) \quad (8)$$

where t_{\min} is the minimum chip thickness, r is the tool edge radius, and ρ is the friction angle between the tool and the workpiece.

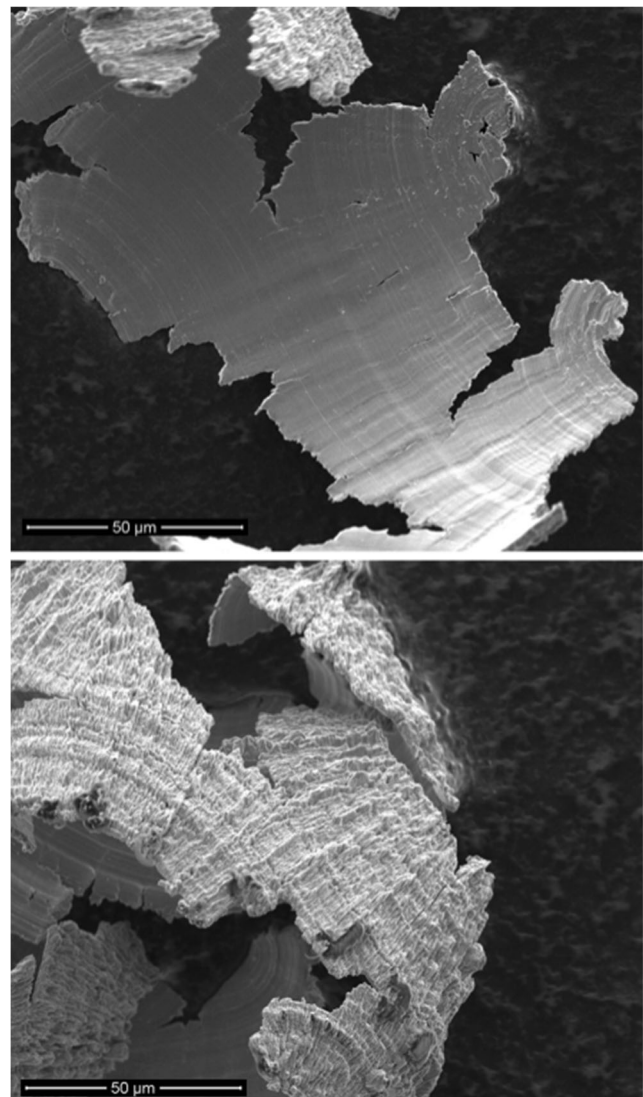
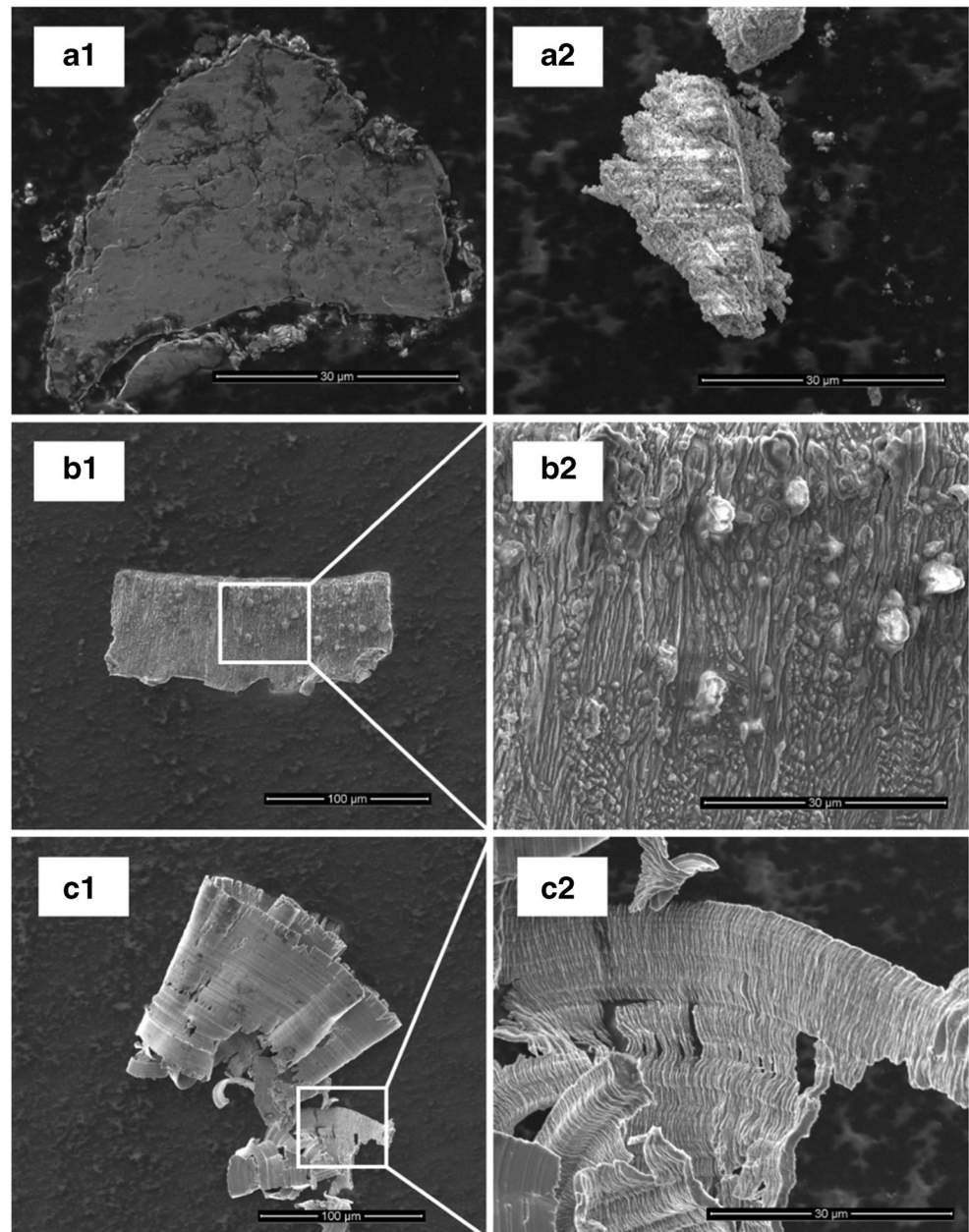


Fig. 14 SEM micrographs of torn chip at $h_{\max} = 99$ nm

Fig. 15 SEM micrographs of chips generated at $h_{\max} = 10$ nm ((a1, (a2)), 30 nm ((b1), (b2)), and 50 nm ((c1), (c2))



The friction angle can be obtained by Eq. (9) [41]:

$$\rho = \alpha + \tan^{-1} \frac{F_t}{F_c} \quad (9)$$

where α is rake angle ($\alpha = 0$ in this study) and F_t and F_c are the two force components which are easily measured when the undeformed chip thickness is far larger than the tool edge radius. In this study, using the relationship of principal and thrust forces captured at $h_{\max} = 12,331$ nm, a minimum uncut chip thickness was calculated to be 10.71 nm, which is roughly in agreement with experimental results.

Next, the chip tearing ratio (r_{ct}), which is the ratio of the torn parts of chip formed under undeformed chip thickness of

100 nm to the total width of chip, was calculated. Figure 16 presents the results of r_{ct} factor. The r_{ct} shows the same trend as that of specific cutting force shown in Fig. 11, indicating the correlation of these two factors.

The detailed calculation procedures of the length of edge where thickness is less than a value and chip tearing ratio (r_{ct}) are given in the Appendix of this paper.

3.3 Surface topography and hardness change

Surface roughness was measured in three-dimensional forms in which the average arithmetical deviation of area (S_a) was calculated by using the TalyMap software. The S_a data

recorded according to feed rate and depth of cut during experiments are presented in Fig. 17. From this figure, it can be seen that S_a decreases as undeformed chip thickness decreases. A surface roughness of 47 nm was obtained at a feed rate of 10 $\mu\text{m}/\text{rev}$. However, an inverse trend is observed at a feed rate lower than 10 $\mu\text{m}/\text{rev}$.

In order to find out the reasons for the changes in S_a , SEM observations and three-dimensional topography measurements of machined surfaces were performed for each cutting condition. Figure 18 shows SEM micrographs and three-dimensional topographies of machined surfaces at three different feed rates. At high feed rate (100 $\mu\text{m}/\text{rev}$), the surface roughness is attributed to the feed marks. When the tool feed rate is smaller than 10 $\mu\text{m}/\text{rev}$, however, no tool feed marks are seen. The surface roughness is due to non-periodical unevenness and surface protrusions.

Further examinations of machined surface samples show that apart from tool feed marks, there are other types of features influencing surface roughness, including material plucking from workpiece surface, debris, scratches, and adhered chips. As shown in Fig. 18, extremely small debris and scratches are observed under all different feed rates. Plucking of material from surface is observed at a higher feed rate (Fig. 19(a)), whereas chip adhesion was observed remarkably on machined surface at lower tool feed rate (Fig. 19(b)).

There might be two reasons for plucking. First, a small part of workpiece material was peel off from its original surface by the flank face of the tool. Second, built-up edges were formed which produces unstable cutting and deep material removal [20]. Scratches might be a result of replication of the micro chippings on the tool edge. The adhered chips on machined surface are presumably due to the chip tearing phenomenon, as described in Section 3.2. Due to the high pressure toward the workpiece surface at an extremely small undeformed chip thickness, a part of material cannot be completely removed as chip and instead, remained on the surface as material adhesion. In addition, debris on the machined surface might also be a part of material separated from torn chips.

To illustrate the effect of high pressure on the deposition of torn chips on machined surface, FE modeling were performed

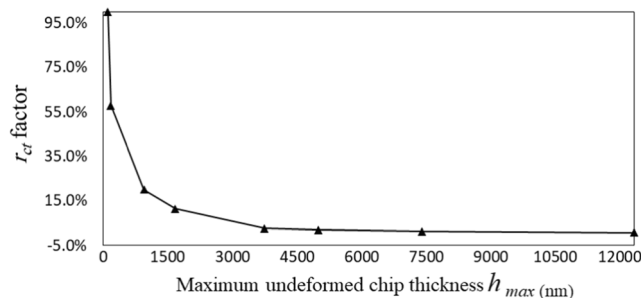


Fig. 16 Change of r_{ct} with h_{max}

at two different depths of cut. At a large depth of cut (Fig. 20(a)), high pressure only exists in small regions of chip. At a small depth of cut (Fig. 20(b)), however, cutting pressure affects all chip thicknesses. Such a high pressure acting at very fine chip thickness provides condition for some parts of chips to stick on surface.

Figure 21 shows the back side of a chip formed at $h_{max} = 172$ nm. Some parts of chip have been detached, leaving holes on the chip. The detached parts of chips might become debris or chip adhesion onto the machined surface.

In addition, cutting at low undeformed chip thickness has great influences on the subsurface microstructure of workpiece. As shown in Fig. 20(b), decreasing depth of cut will increase residual stress on a machined surface. To verify this effect, the Vickers hardness of the machined surface was measured. As shown in Table 2, the Vickers hardness exhibits a 15 to 30% increase after machining compared to that before machining (145 HV, Table 1).

3.4 Tool wear and material adhesion

Figure 22 shows SEM micrographs of the tool after cutting of titanium for a cutting distance of 75 and 250 m. The h_{max} was changed from 99 to 12,331 nm during this cutting distance; 96% of the cutting distance was performed at a maximum undeformed chip thickness of less than 500 nm. As shown in Fig. 22((a1), (a2), (a3)), after just 75 m cutting, chips were welded to the tool rake face. In nanometer-scale ultraprecision machining, pressure significantly increases compared to traditional machining, which promotes material adhesion on tool. As the cutting distance increases (Fig. 22((b1), (b2), (b3))), both the rake and flank faces are covered by titanium adhesion, although the appearances of

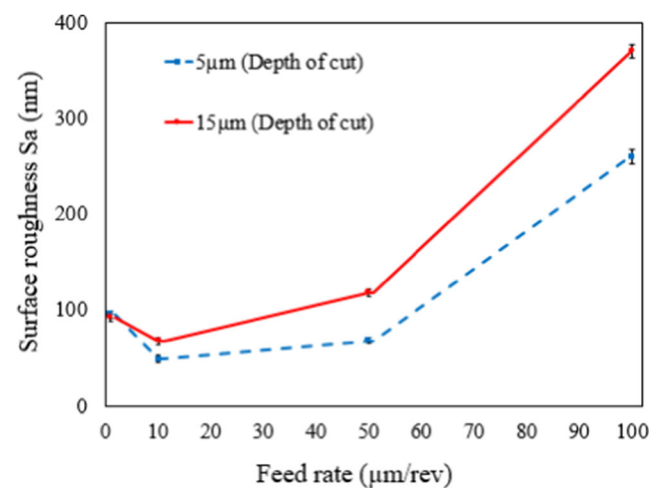


Fig. 17 Surface roughness (S_a) of machined surface at different feed rates and depths of cut

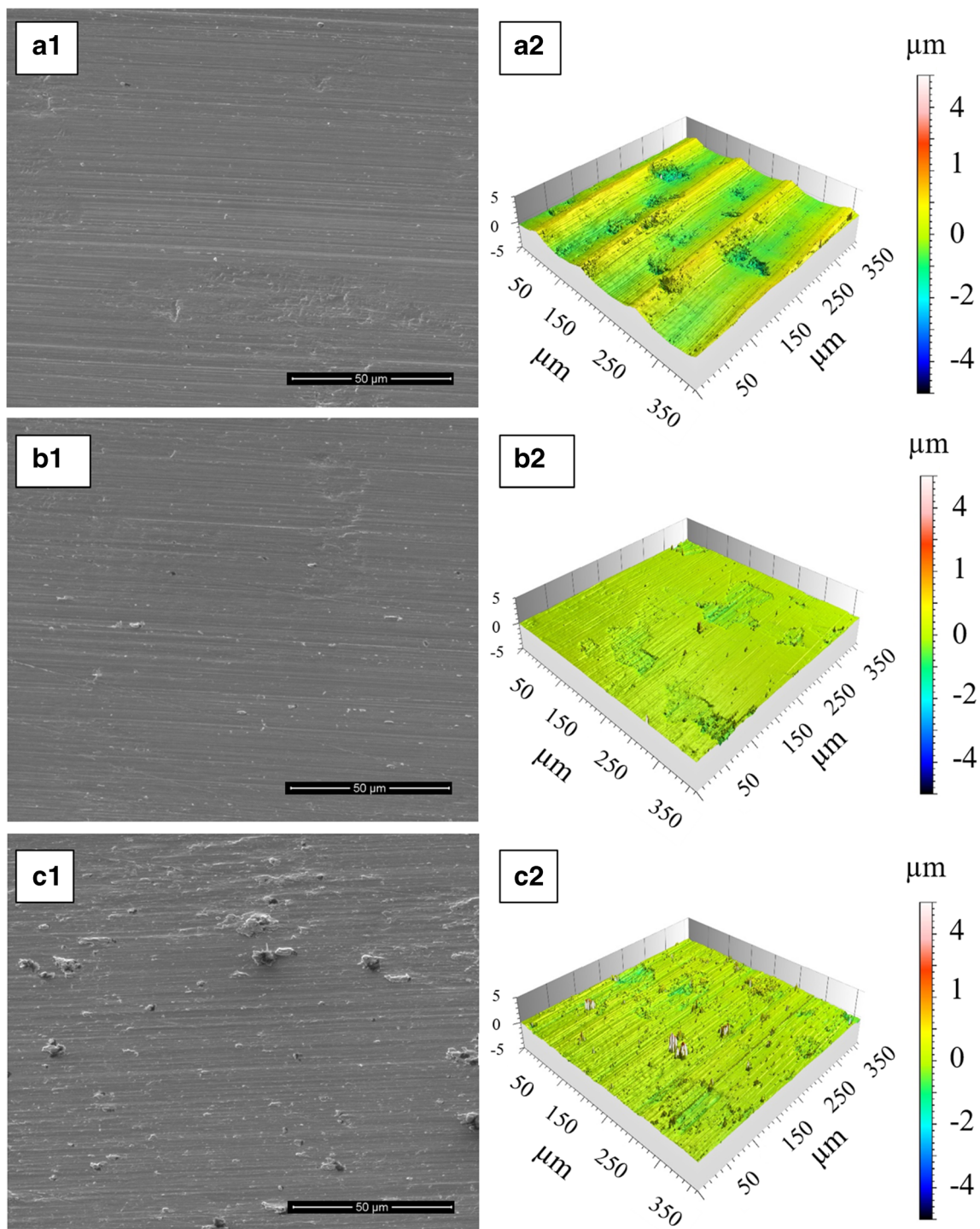
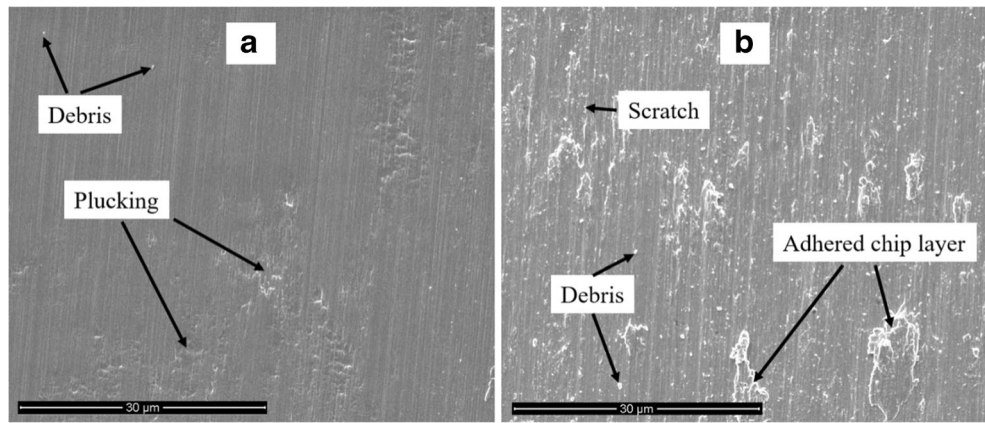


Fig. 18 SEM micrographs and three-dimensional surface topographies of machined surfaces at $f=100\ \mu\text{m}/\text{rev}$ ($h_{\text{max}}=12,331\ \text{nm}$) (a1, a2), $f=10\ \mu\text{m}/\text{rev}$ ($h_{\text{max}}=1676\ \text{nm}$) (b1, b2), and $f=1\ \mu\text{m}/\text{rev}$ ($h_{\text{max}}=172\ \text{nm}$) (c1, c2)

adhesion are different. At the same time, built-up edges are found on the rake face side. Small flank wear lands and a few micro chippings are also observed around the tool edge. As tool wear increases, tool edge geometry will change, leading to change in chip morphology, as shown in Fig. 12.

Yang and Richard [6] indicated the high stress generated in machining titanium is one of main reasons for the rapid wear of tools. Zlatin and Field [42] have found that titanium chips have a strong tendency to weld to the cutting edge, particularly after the tool starts to wear. A localized region of high pressure at the tool-

Fig. 19 SEM micrographs of machined surfaces at $h_{\max} = 12,331 \text{ nm}$ ((a)) and $h_{\max} = 172 \text{ nm}$ ((b))



workpiece interface also increases the reactivity of titanium. The wear of a diamond tool is attributed to graphitization of diamond [12, 21, 43, 44]. Qian et al. [45] proved that contact pressure is an important parameter for diamond-graphite transformation. Liu et al. [46] reported that TiC synthesis occurs when titanium and graphite are interacted under high temperature and pressure.

Figure 22((b1)) further shows that the width of flank wear land increases from right side to left side. As shown in Fig. 9, the left side of tool corresponds to the small undeformed chip thickness area (“I” in Fig. 9), where flank face wear is significant. For the right side corresponding to “II” in Fig. 9, material adhesion on rake face

is more significant. With increasing tool wear, the tool-workpiece contact area is increased due to reduced clearance angle, which creates more rubbing of the workpiece surface [18]. The built-up layer that is formed on the tool flank face can push the tool off from its original route to increase the surface roughness [47].

4 Conclusions

The chip formation behavior of pure titanium in nanometer-scale ultraprecision diamond turning tests was investigated by both experiments and FE simulation. The following conclusions were obtained:

- (1) There are remarkable changes in shear angle (around 90% decrease) and specific cutting force (about 300%

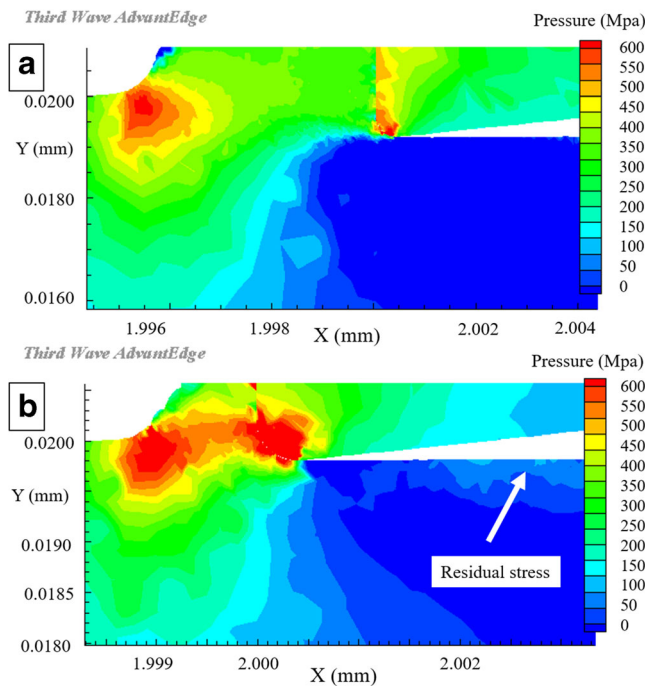


Fig. 20 FE simulation of pressure distributions at $a = 2.0 \times r$ (a) and $a = 0.5 \times r$ (b)

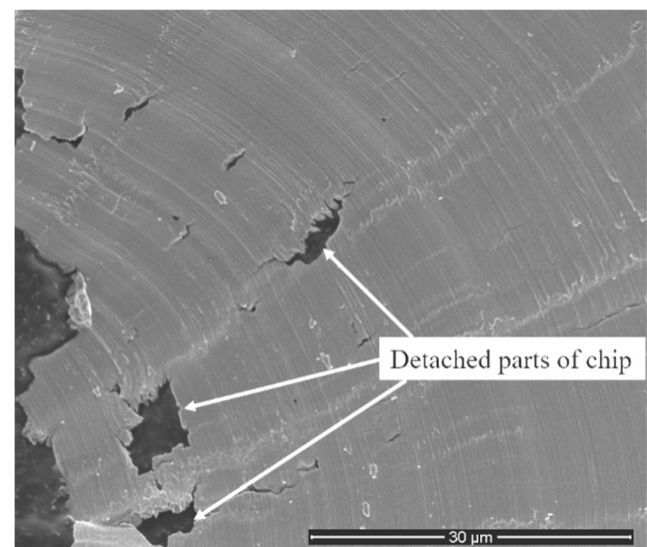


Fig. 21 SEM micrograph of the detached parts of a chip

Table 2 Vickers hardness (HV) of workpiece after cutting

<i>a</i>	<i>f</i>			
	1 μm/rev	10 μm/rev	50 μm/rev	100 μm/rev
5 μm	181	191	188	192
15 μm	170	184	179	190

increase) as undeformed chip thickness decreases from the micrometer scale to the nanometer scale.

- (2) As unformed chip thickness decreases down to a critical value (~ 100 nm), chip edge tearing becomes significant. The ratio of chip tearing shows the same trend as the specific cutting force.
- (3) At an extremely small undeformed chip thickness, tool feed mark is no longer a major factor of surface roughness. Instead, material plucking from workpiece surface, debris, scratches, and chip adhesion become important factors. Chip tearing is a main reason for debris generation and chip adhesion.
- (4) The Vickers hardness of workpiece surface exhibits a 15 to 30% increase after machining compared to that before machining.
- (5) Flank wear, micro chipping, and material adhesion on tool surfaces are significant when cutting distance increases, and the significance of each depends on the position on the tool edge.

Appendix 1 Calculation of chip tearing ratio (r_{ct})

Figure 23(a, b) shows schematic illustration of undeformed chip area at two different feed rates.

To calculate the length of chip edge (where thickness is less than a desired value) on the “I” edge as shown in Fig. 23(a), first, using Eq. (1), depth of cut at which chip thickness equals the desired value can be obtained; then, this depth of cut can be applied in following equations to calculate the length of chip edge in “I” side as shown in Fig. 23(a).

$$L_1 = 2\pi R \times \left(\frac{\alpha + \beta}{360} \right) \quad (\text{A.1})$$

$$\alpha = \arctan \left(\frac{\sqrt{2R-a^2}}{R-a} \right) \quad (\text{A.2})$$

$$\beta = \arctan \left(\frac{\frac{f}{2}}{\sqrt{R^2 - \left(\frac{f}{2}\right)^2}} \right) \quad (\text{A.3})$$

When depth of cut calculated by Eq. (1) is less than a critical value, which is unique for every feed rate and tool nose radius, Eq. (A.1) is no longer valid. This critical value can be calculated using $f = \sqrt{2Ra - a^2}$ which means $y = 0$ and h_{\max} is equal to the depth of cut (a) as shown in

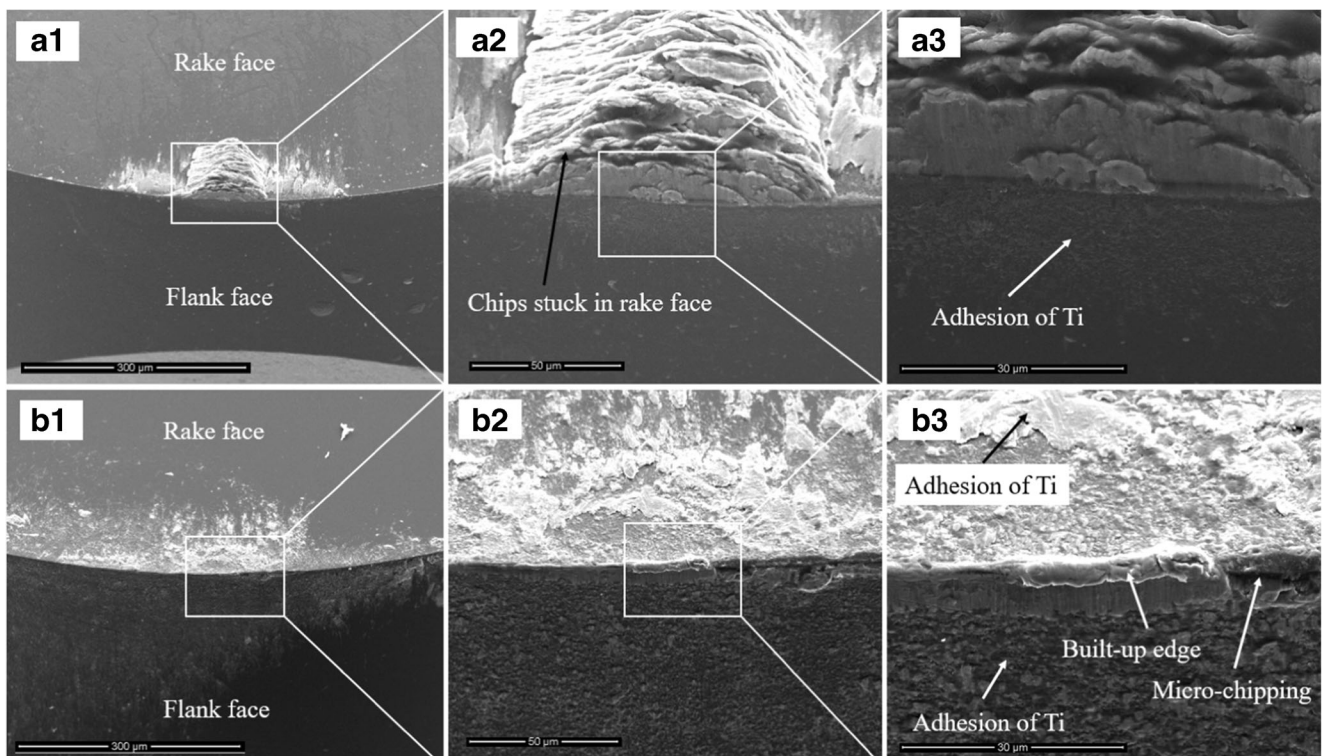


Fig. 22 SEM micrographs of tool after a cutting distance of 75 m ((a1)–(a3)) and 250 m ((b1)–(b3))

Fig. 23 Schematic model for critical thickness on chip edges at two different feed rates

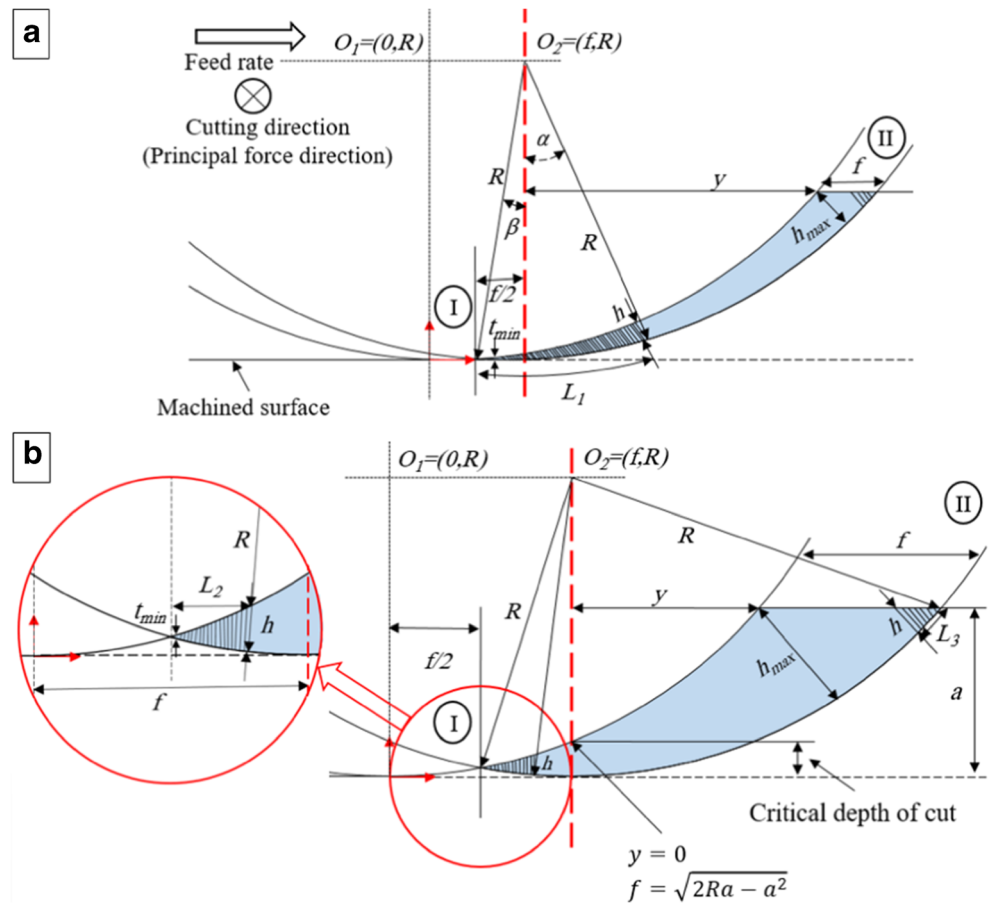


Fig. 23(b). This critical depth of cut at feed rate of 50 and 100 $\mu\text{m}/\text{rev}$ is 1.25 and 5.0 μm , while thickness required is less than 100 nm. As a result, the starting point of edge tearing is somewhere in the left side of critical depth of cut (red dash line) as shown in Fig. 23(b). In this case, length of chip edge can be calculated using following equation.

$$L_2 = \sqrt{R^2 - (R-a)^2} - \frac{f}{2} \tag{A.4}$$

To calculate the length of chip edge on the “II,” the following equation can be used at all feed rates:

$$L_3 = \sqrt{f^2 - h^2} \tag{A.5}$$

In order to calculate the total width of chip, the target value can be set to be h_{max} in Eq. (1), and then using Eq. (A.1), the total width of chip will be obtained.

References

- Boyer R, Welsch G, Collings EW (1993) Materials properties handbook: titanium alloys. ASM international
- Davim JP (2014) Machining of titanium alloys. doi: <https://doi.org/10.1007/978-3-662-43902-9>
- Ezugwu EO, Wang ZM (1997) Titanium alloys and their machinability—a review. J Mater Process Technol 68:262–274. [https://doi.org/10.1016/S0924-0136\(96\)00030-1](https://doi.org/10.1016/S0924-0136(96)00030-1)
- Machado AR, Wallbank J (1990) Machining of titanium and its alloys—a review. Proc Inst Mech Eng Part B J Eng Manuf 204:53–60. https://doi.org/10.1243/PIME_PROC_1990_204_047_02
- Matthew J, Donachie J (2012) Titanium a technical guide, 2nd ed. ASM Int doi: <https://doi.org/10.5772/1844>
- Yang X, Richard Liu C (1999) Machining titanium and its alloys. Mach Sci Technol 3:107–139. <https://doi.org/10.1080/10940349908945686>
- Sun S, Brandt M, Dargusch MS (2009) Characteristics of cutting forces and chip formation in machining of titanium alloys. Int J Mach Tools Manuf 49:561–568. <https://doi.org/10.1016/j.ijmachtools.2009.02.008>
- Calamaz M, Coupard D, Girot F (2008) A new material model for 2D numerical simulation of serrated chip formation when machining titanium alloy Ti–6Al–4V. Int J Mach Tools Manuf 48:275–288. <https://doi.org/10.1016/j.ijmachtools.2007.10.014>
- Molinari A, Soldani X, Miguez MH (2013) Adiabatic shear banding and scaling laws in chip formation with application to cutting of Ti–6Al–4V. J Mech Phys Solids 61:2331–2359. <https://doi.org/10.1016/j.jmps.2013.05.006>
- Komanduri R, Von Turkovich BF (1981) New observations on the mechanism of chip formation when machining titanium alloys. Wear 69:179–188. [https://doi.org/10.1016/0043-1648\(81\)90242-8](https://doi.org/10.1016/0043-1648(81)90242-8)

11. Komanduri R (1982) Some clarifications on the mechanics of chip formation when machining titanium alloys. *Wear* 76:15–34. [https://doi.org/10.1016/0043-1648\(82\)90113-2](https://doi.org/10.1016/0043-1648(82)90113-2)
12. Ezugwu EO, Bonney J, Yamane Y (2003) An overview of the machinability of aeroengine alloys. *J Mater Process Technol* 134:233–253. [https://doi.org/10.1016/S0924-0136\(02\)01042-7](https://doi.org/10.1016/S0924-0136(02)01042-7)
13. Hasçalık A, Çaydaş U (2008) Optimization of turning parameters for surface roughness and tool life based on the Taguchi method. *Int J Adv Manuf Technol* 38:896–903. <https://doi.org/10.1007/s00170-007-1147-0>
14. Ramesh S, Karunamoorthy L, Palanikumar K (2008) Fuzzy modeling and analysis of machining parameters in machining titanium alloy. *Mater Manuf Process* 23:439–447. <https://doi.org/10.1080/10426910801976676>
15. Chauhan SR, Dass K (2012) Optimization of machining parameters in turning of titanium (grade-5) alloy using response surface methodology. *Mater Manuf Process* 27:531–537. <https://doi.org/10.1080/10426914.2011.593236>
16. Ribeiro MV, Moreira MRV, Ferreira JR (2003) Optimization of titanium alloy (6Al-4V) machining. *J Mater Process Technol* 143–144:458–463. [https://doi.org/10.1016/S0924-0136\(03\)00457-6](https://doi.org/10.1016/S0924-0136(03)00457-6)
17. Che-Haron CH (2001) Tool life and surface integrity in turning titanium alloy. *J Mater Process Technol* 118:231–237. [https://doi.org/10.1016/S0924-0136\(01\)00926-8](https://doi.org/10.1016/S0924-0136(01)00926-8)
18. Ulutan D, Ozel T (2011) Machining induced surface integrity in titanium and nickel alloys: a review. *Int J Mach Tools Manuf* 51:250–280. <https://doi.org/10.1016/j.ijmactools.2010.11.003>
19. Che-Haron CH, Jawaid A (2005) The effect of machining on surface integrity of titanium alloy Ti-6% Al-4% V. *J Mater Process Technol* 166:188–192. <https://doi.org/10.1016/j.jmatprotec.2004.08.012>
20. Ginting A, Nouari M (2009) Surface integrity of dry machined titanium alloys. *Int J Mach Tools Manuf* 49:325–332. <https://doi.org/10.1016/j.ijmactools.2008.10.011>
21. Zareena AR, Veldhuis SC (2012) Tool wear mechanisms and tool life enhancement in ultraprecision machining of titanium. *J Mater Process Technol* 212:560–570. <https://doi.org/10.1016/j.jmatprotec.2011.10.014>
22. Schneider F, Lohkamp R, Sousa FJP et al (2014) Analysis of the surface integrity in ultraprecision cutting of cp-titanium by investigating the chip formation. *Procedia CIRP* 13:55–60. <https://doi.org/10.1016/j.procir.2014.04.010>
23. Schneider F, Bischof R, Kirsch B et al (2016) Investigation of chip formation and surface integrity when micro-cutting cp-titanium with ultra-fine grain cemented carbide. *Procedia CIRP* 45:115–118. <https://doi.org/10.1016/j.procir.2016.02.257>
24. Ruibin X, Wu H (2016) Study on cutting mechanism of Ti6Al4V in ultraprecision machining. *Int J Adv Manuf Technol* 86:1311–1317. <https://doi.org/10.1007/s00170-015-8304-7>
25. Colafemina JP, Jasinevicius RG, Duduch JG (2007) Surface integrity of ultraprecision diamond turned Ti (commercially pure) and Ti alloy (Ti-6Al-4V). *Proc Inst Mech Eng Part B J Eng Manuf* 221:999–1006. <https://doi.org/10.1243/09544054JEM798>
26. Liu K, Li XP, Rahman M et al (2007) A study of the effect of tool cutting edge radius on ductile cutting of silicon wafers. *Int J Adv Manuf Technol* 32:631–637. <https://doi.org/10.1007/s00170-005-0364-7>
27. Heidari M, Yan J (2017) Ultraprecision surface flattening of porous silicon by diamond turning. *Precis Eng* 49:262–277. <https://doi.org/10.1016/j.precisioneng.2017.02.015>
28. Lalwani DI, Mehta NK, Jain PK (2008) Experimental investigations of cutting parameters influence on cutting forces and surface roughness in finish hard turning of MDN250 steel. *J Mater Process Technol* 206:167–179. <https://doi.org/10.1016/j.jmatprotec.2007.12.018>
29. de Oliveira FB, Rodrigues AR, Coelho RT, de Souza AF (2015) Size effect and minimum chip thickness in micromilling. *Int J Mach Tools Manuf* 89:39–54. <https://doi.org/10.1016/j.ijmactools.2014.11.001>
30. Rao BC, Shin YC (1999) A comprehensive dynamic cutting force model for chatter prediction in turning. *Int J Mach Tools Manuf* 39:1631–1654. [https://doi.org/10.1016/S0890-6955\(99\)00007-3](https://doi.org/10.1016/S0890-6955(99)00007-3)
31. Chae J, Park SS, Freiheit T (2006) Investigation of micro-cutting operations. *Int J Mach Tools Manuf* 46:313–332. <https://doi.org/10.1016/j.ijmactools.2005.05.015>
32. Klocke F (2011) Manufacturing processes 1: cutting. doi: <https://doi.org/10.1007/978-3-642-11979-8>
33. Grzesik W (2008) Advanced machining processes of metallic materials: theory, modelling and applications. Elsevier
34. Liu X, DeVor RE, Kapoor SG, Ehmann KF (2004) The mechanics of machining at the microscale: assessment of the current state of the science. *J Manuf Sci Eng* 126:666. <https://doi.org/10.1115/1.1813469>
35. Ikawa N, Shimada S, Tanaka H (1992) Minimum thickness of cut in micromachining. *Nanotechnology* 3:6–9. <https://doi.org/10.1088/0957-4484/3/1/002>
36. Lai X, Li H, Li C et al (2008) Modelling and analysis of micro scale milling considering size effect, micro cutter edge radius and minimum chip thickness. *Int J Mach Tools Manuf* 48:1–14. <https://doi.org/10.1016/j.ijmactools.2007.08.011>
37. Malekian M, Mostofa MG, Park SS, Jun MBG (2012) Modeling of minimum uncut chip thickness in micro machining of aluminum. *J Mater Process Technol* 212:553–559. <https://doi.org/10.1016/j.jmatprotec.2011.05.022>
38. Zhanqiang L, Zhenyu S, Yi W (2013) Definition and determination of the minimum uncut chip thickness of microcutting. *Int J Adv Manuf Technol* 69:1219–1232. <https://doi.org/10.1007/s00170-013-5109-4>
39. Elkaseer A, Dimov S, Pham D, et al (2016) Material microstructure effects in micro-endmilling of Cu99.9E. *Proc Inst Mech Eng Part B J Eng Manuf*. doi: <https://doi.org/10.1177/0954405416666898>
40. Son SM, Lim HS, Ahn JH (2005) Effects of the friction coefficient on the minimum cutting thickness in micro cutting. *Int J Mach Tools Manuf* 45:529–535. <https://doi.org/10.1016/j.ijmactools.2004.09.001>
41. Altintas Y (2012) Manufacturing automation: metal cutting mechanics, machine tool vibrations, and CNC design, second edn. Cambridge University Press, New York
42. Zlatin N, Field M (1973) Procedures and precautions in machining titanium alloys. In: Jaffee RI, Burte HM (eds) *Titan Sci Technol*. Springer US, Boston, MA, pp 489–504
43. Thornton AG, Wilks J (1979) Tool wear and solid state reactions during machining. *Wear* 53:165–187. [https://doi.org/10.1016/0043-1648\(79\)90226-6](https://doi.org/10.1016/0043-1648(79)90226-6)
44. Kohlscheen J, Stock H-R, Mayr P (2002) Tailoring of diamond machinable coating materials. *Precis Eng* 26:175–182. [https://doi.org/10.1016/S0141-6359\(01\)00109-X](https://doi.org/10.1016/S0141-6359(01)00109-X)
45. Qian J, Pantea C, Voronin G, Zerda TW (2001) Partial graphitization of diamond crystals under high-pressure and high-temperature conditions. *J Appl Phys* 90:1632–1637. <https://doi.org/10.1063/1.1382832>
46. Liu H, Wang L, Wang A et al (1997) Preparation of nanometer size TiC particulate reinforcements in Ti matrix composites under high pressure. *Nanostructured Mater* 9:177–180. [https://doi.org/10.1016/S0965-9773\(97\)00047-0](https://doi.org/10.1016/S0965-9773(97)00047-0)
47. Mantle AL, Aspinwall DK (1997) Surface integrity and fatigue life of turned gamma titanium aluminide. *J Mater Process Technol* 72:413–420. [https://doi.org/10.1016/S0924-0136\(97\)00204-5](https://doi.org/10.1016/S0924-0136(97)00204-5)